Small

NANO · MICRO small
www.small-journal.com

RESEARCH ARTICLE OPEN ACCESS

Electrostatic Regulation of Sulfur Spatial Evolution for Dimensionally Stable Lithium–Sulfur Batteries

Ting-Yu Hsu[1] | Yu-Teng Tsai[2] | Yu-Ting Chiu[1] | Ching-Yu Tung[2] | Ching-Yu Chiang[3] | Elise Yu-Tzu Li[2] | Yu-Sheng Su[1,4]

[1]International College of Semiconductor Technology, National Yang Ming Chiao Tung University, Hsinchu, Taiwan | [2]Department of Chemistry, National Taiwan Normal University, Taipei, Taiwan | [3]National Synchrotron Radiation Research Center, Hsinchu, Taiwan | [4]Industry Academia Innovation School, National Yang Ming Chiao Tung University, Hsinchu, Taiwan

Correspondence: Elise Yu-Tzu Li (eliseytli@ntnu.edu.tw) | Yu-Sheng Su (yushengsu@nycu.edu.tw)

Received: 10 June 2026 | **Revised:** 7 August 2026 | **Accepted:** 3 September 2026

Keywords: Bader charge analysis | DFT simulations | electrode swelling | nano-XRF mapping | polysulfide conversion kinetics | spatial sulfur redistribution

ABSTRACT

Lithium–sulfur (Li–S) batteries are promising for high-energy storage but are limited by complex multistep sulfur redox reactions that induce polysulfide migration, sluggish conversion kinetics, and severe cathode swelling. Here, we report a boron nitride/carbon nanotube (BN/CNT) heterostructure that enables electrostatic regulation of sulfur spatial evolution through the separation of polar domains and conductive networks. The conductive CNT scaffold preserves electron percolation, whereas the BN interlayer provides abundant polarity to regulate polysulfide interactions. Amine functionalization (BN–NH_2) further tailors the local electronic environment and interfacial charge distribution. Consequently, sulfur spatial evolution is regulated toward homogeneous redistribution rather than surface overaccumulation, resulting in near-zero cathode swelling during prolonged cycling. The optimized BN–NH_2/CNT configuration maintains a capacity of 1150 mAh g^{-1} after 500 cycles and exhibits reduced polarization and enhanced rate capability. Potentiostatic nucleation analysis, nano-X-ray fluorescence mapping, depth-resolved X-ray photoelectron spectroscopy, and X-ray absorption spectroscopy reveal stabilized sulfur redox chemistry and regulated sulfur electronic environments. Density functional theory calculations reveal interfacial charge redistribution and optimized interaction strengths that support regulated sulfur redox chemistry. In this work, moderated electrostatic regulation of sulfur spatial evolution is established as a design principle for dimensionally stable and kinetically optimized Li–S cathodes beyond adsorption-centric strategies.

1 | Introduction

Lithium–sulfur (Li–S) batteries are widely regarded as promising candidates for next-generation energy storage owing to their high theoretical energy density and the abundance of sulfur. Nevertheless, their practical realization remains limited by the complex redox chemistry of sulfur, which involves the formation and redistribution of soluble lithium polysulfides (Li_2S_x; $4 \leq x \leq 8$) [1, 2]. The dissolution, migration, and repeated deposition of these species not only induce shuttle effects and sluggish reaction kinetics but also result in continuous structural reorganization of the cathode [3]. Beyond polysulfide shuttling, electrode swelling and nonuniform sulfur redistribution represent persistent yet often overlooked issues in Li–S systems [4]. During cycling, soluble intermediates tend to accumulate near the electrode surface, forming dense and electronically insulating deposits that hinder ion and electron transport. Such surface-dominated deposition can lead to progressive thickness expansion, loss of spatial homogeneity, and mechanical instability of the cathode architecture. While numerous studies focus on enhancing the

This is an open access article under the terms of the Creative Commons Attribution License, which permits use, distribution and reproduction in any medium, provided the original work is properly cited.
© 2026 The Author(s). *Small* published by Wiley-VCH GmbH

polysulfide adsorption strength, far less attention has been given to how interfacial regulation governs the spatial sulfur distribution and dimensional stability of cathodes.

The introduction of polar host materials has been widely explored to immobilize polysulfide intermediates [2, 5, 6]. However, excessively strong chemical binding may increase reaction barriers, impede reversible Li_2S formation–decomposition processes, and disrupt conductive pathways [7–9]. These findings suggest that effective sulfur host design requires not only strong adsorption but also moderated electrostatic regulation that balances polysulfide confinement, charge transport, and structural stability. Hexagonal boron nitride (BN), possessing intrinsic polarity from B–N bonds, offers tunable electrostatic interactions with sulfur species. However, its insulating nature necessitates rational architectural design to preserve electronic percolation. In this work, we construct a bilayer BN/CNT heterostructure that spatially separates conductive and polar domains, enabling interfacial regulation while maintaining electron transport continuity. Furthermore, amine functionalization (BN–NH_2) is introduced to tailor the local electronic environment and fine-tune electrostatic interactions with polysulfides.

Through integrated electrochemical analysis, potentiostatic Li_2S nucleation measurements, nano-X-ray fluorescence (XRF) mapping, depth-resolved X-ray photoelectron spectroscopy (XPS), and S K-edge X-ray absorption spectroscopy (XAS), we demonstrate that moderated electrostatic regulation promotes homogeneous sulfur redistribution, suppresses surface overaccumulation, and mitigates electrode swelling. The resulting cathode exhibits a dimensionally stable architecture and enhanced active sulfur utilization during prolonged cycling. This work highlights the importance of spatial and electronic regulation in designing structurally robust Li–S cathodes beyond conventional adsorption-centric strategies.

2 | Results and Discussion

2.1 | Structural and Chemical Design of Amine-Functionalized BN/CNT Heterostructures

To verify the successful construction of the heterostructured architecture, the structural integration of BN with the CNT framework was first examined. As shown in Figures 1a and S2, the pristine CNT film consists of an interconnected and porous nanotube network, providing a continuous conductive scaffold [10]. XRD of the CNT substrate reveals a characteristic graphitic (002) reflection at $2\theta \approx 25.8°$ (Figure S3), whereas the Raman spectrum displays typical D and G bands with an I_D/I_G ratio of 1.17 (Figure S4), indicating a defect-rich carbon framework [10, 11]. Following BN incorporation, the SEM images shown in Figure 1b reveal that the BN nanosheet materials (Figure 1c) are uniformly distributed over the CNT surface, resulting in the formation of a bilayer heterostructure. Correspondingly, elemental mapping (Figure 1d) confirms the homogeneous distribution of B, N, and C across the film. The XRD patterns (Figure 1e) show a dominant diffraction peak at $2\theta \approx 26.7°$ that is characteristic of the (002) plane of hexagonal BN [12]. Compared with those of the bulk BN powder, higher-order reflections such as (100), (101), (102), (110), and (112) are significantly suppressed in the BN/CNT heterostructure, while the (002) peak remains prominent. Such evolution suggests a possible preferential alignment of BN nanosheets with their basal planes parallel to the substrate surface [13]. In addition, the (002) reflection of the CNT becomes indistinguishable in the heterostructure, indicating that the diffraction signal is largely dominated by BN after integration. In agreement with the XRD results, the Raman spectra (Figure 1f) show that bulk BN exhibits a characteristic E_2g mode at 1357.4 cm^{-1}, whereas the BN/CNT heterostructure displays a redshift of ~3 cm^{-1} [14, 15]. This subtle shift suggests a slight modulation of interlayer coupling, which may be associated with mechanical processing and heterointerface formation [14, 15]. Upon amine functionalization, no discernible lattice distortion is observed, as evidenced by the preserved (002) diffraction peak of BN (Figure S5) and the absence of further Raman shifts. The FTIR spectra (Figure 1g) display the characteristic B–N vibrational modes at ~1370 cm^{-1} (in-plane B–N stretching) and ~772 cm^{-1} (out-of-plane B–N bending), confirming the preservation of the BN framework [16, 17]. Moreover, additional N–H-related vibrational features are observed, indicating successful amine incorporation [16, 17]. High-resolution XPS analysis further revealed a slight positive shift (+0.2 eV) for the B–N bond (190.4 eV) in the B 1s spectrum and an increased relative intensity of the N–H peak (~399.9 eV) in the N 1s region (Figure 1h–j) [18, 19], suggesting a slight redistribution of the local electronic environment following amine treatment.

2.2 | Theoretical Insights into Electrostatic Interfacial Regulation

The optimized structures of soluble LiPSs (Li_2S_3, Li_2S_4, Li_2S_6, and Li_2S_8) and the substrate surfaces, including graphene (GN) on CNT, the boron nitride/graphene bilayer (BN/GN), and the NH_2-functionalized boron nitride/graphene heterostructure (BN–NH_2/GN), are shown in Figure 2. The optimized interlayer distance between GN and BN (or BN–NH_2) is approximately 3.50 Å. As shown in Figure S6, the electrostatic potential (ESP) maps reveal a strong negative potential localized on the surface amine (–NH_2) and a positive potential on the Li atoms of the LiPSs. The distinct potential alignment provides direct visual evidence of long-range dipole–dipole electrostatic attraction, which actively regulates and anchors the LiPSs prior to physical adsorption or chemical bonding. Additionally, Figure 3 summarizes the adsorption configurations and energies of lithium polysulfides on these surfaces. The results clearly indicate that the surface composition significantly influences the adsorption capacity. For pristine GN, adsorption is governed mainly by van der Waals interactions, which are characteristic of physisorption. In contrast, BN/GN exhibits enhanced interactions with adsorbates because of the polarity of the B–N bonds. This interaction can be described primarily as an electrostatic interaction between Li^+ species and polarized nitrogen sites. Upon further functionalization with NH_2 groups, the interaction strength is increased, reflecting strengthened yet regulated interfacial interactions with tunable chemisorption characteristics rather than irreversible strong binding. Such tuned interactions are expected to facilitate reversible polysulfide conversion by maintaining proximity to conductive pathways without the introduction of excessive barriers to bonding.

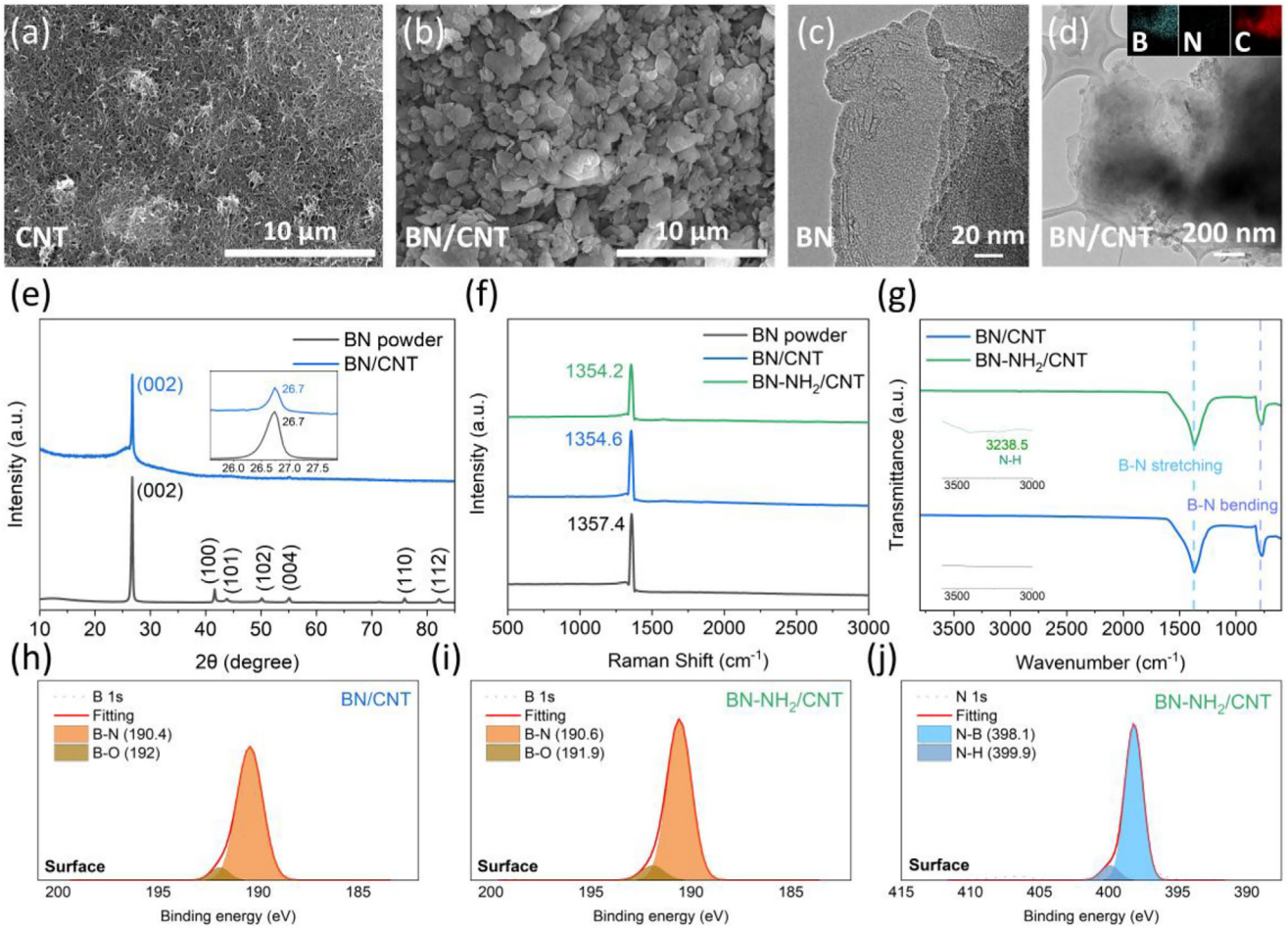


FIGURE 1 | Structural and chemical characterization of the amine-functionalized BN/CNT heterostructures. SEM images of (a) the pristine CNT film and (b) the BN/CNT heterostructure. TEM image of (c) ball-milled BN nanosheets and (d) the BN/CNT heterostructure and the EDS mapping results, confirming the uniform distribution of B, N, and C. (e) XRD patterns of the BN powder and BN/CNT bilayer substrate. (f) Raman spectra showing that, compared with that of bulk BN powder, the E_2g vibrational mode of the BN/CNT heterostructure is redshifted, suggesting subtle modulation of the interlayer coupling and stacking configuration. (g) FTIR spectra displaying the characteristic B–N vibrational modes and confirming amine functionalization through N–H-related vibrational features. XPS B 1s spectra of the (h) BN/CNT and (i) BN–NH_2/CNT substrates. (j) XPS N 1s spectra showing an increased intensity of the N–H related peak at ~399.9 eV after amine functionalization.

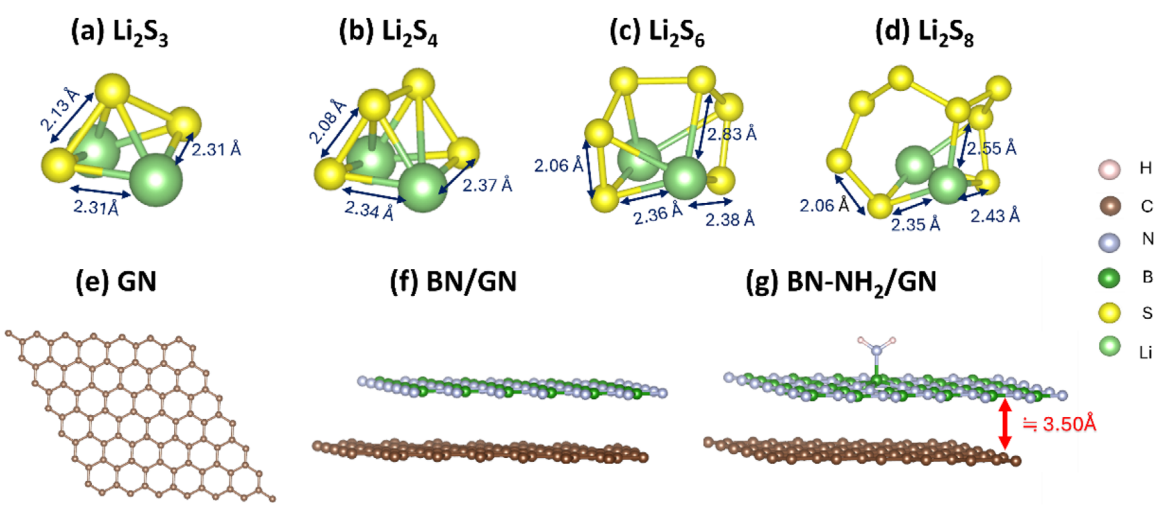


FIGURE 2 | Optimized structures of (a–d) LiPSs (Li_2S_3, Li_2S_4, Li_2S_6, and Li_2S_8) and (e) graphene (GN), representing the CNT surface structure, (f) boron nitride/graphene (BN/GN), and (g) NH_2-functionalized boron nitride/graphene (BN–NH_2/GN). The colors of the atoms are white (H), brown (C), blue (N), green (B), yellow (S), and light green (Li).

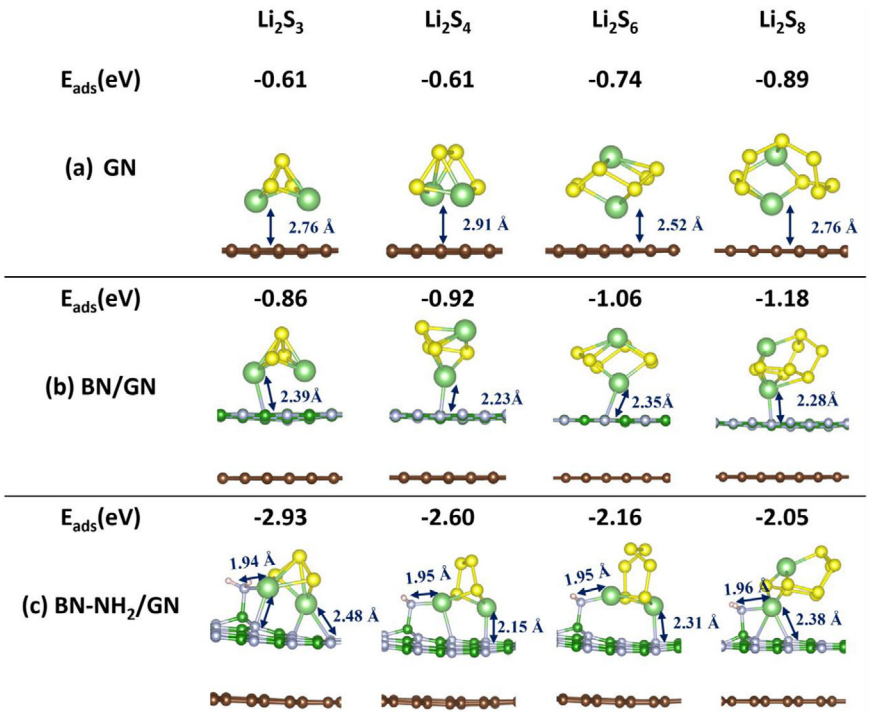


FIGURE 3 | Adsorption configurations and energies (E_{ads}, in eV) of different LiPSs on (a) graphene (GN), (b) boron nitride/graphene (BN/GN), and (c) the NH_2-functionalized boron nitride/graphene (BN–NH_2/GN) surfaces.

While both GN and BN/GN tend to exhibit increasingly stronger adsorption with longer polysulfide chains, which is attributed to enhanced van der Waals interactions with larger molecules, the behavior of the BN–NH_2/GN system differs. In this case, short-chain LiPS species display relatively stronger adsorption, possibly owing to more pronounced interfacial interactions between localized polar sites and greater charge localization on short-chain LiPSs (Figure 3). Bader charge analysis (Figure S7) and the electron density difference (EDD) analysis (Figure S8) further support this observation, revealing greater charge transfer from LiPSs to the NH_2 groups in short-chain species, indicative of strong binding, which aligns with the calculated adsorption energies. Notably, in the BN–NH_2/GN heterostructure, graphene serves as a conductive substrate that maintains stable adsorption configurations.

To better approximate the realistic distribution of NH_2 groups on the BN/GN surface, a second NH_2 group was introduced at different sites on the BN–NH_2/GN surface, as shown in Figure S9a. The distance between the two NH_2 groups and their corresponding relative energies are summarized in Figure S9b. A clear trend emerges: the two NH_2 groups preferentially remain in close proximity, as this configuration minimizes the extent to which the surface electronic structure is perturbed. Such behavior suggests the possible formation of locally clustered functional sites rather than a perfectly uniform distribution, which may introduce spatial heterogeneity in interfacial interaction strength. The three lowest-energy systems, labeled (a), (b), and (c), were further examined for LiPS adsorption (Figure S10). The results indicate that the presence of dual NH_2 groups further enhances the adsorption capability. In the BN–2NH_2/GN model, LiPSs exhibit relatively high adsorption energies across various configurations, which is attributed to the additional polar anchoring sites that strengthen the interactions between LiPSs and the surface, indicating the tunable feature of this design.

To characterize the interaction regimes between the bilayer surfaces and the –NH_2 moieties, we perform a systematic Bader charge analysis on three systems with different NH_2 coverage: 0–NH_2 (BN/GN), 1–NH_2 (BN–NH_2/GN), and 2–NH_2 (BN–2NH_2/GN) in one unit cell. The total Bader charge of LiPSs, bilayer surfaces, and NH_2 functional group moieties are demonstrated in Figure S11. The BN/GN system exhibits weak interaction characterized by minimal charge transfer within 0.2 |e|, indicating that the interaction is dominated by weak physical adsorption rather than chemisorption. The BN–NH_2/GN system demonstrates moderate interaction characterized by an optimal, balanced charge transfer. This system provides sufficient electrostatic attraction to anchor LiPSs without binding them so tightly that subsequent conversion kinetics are hindered. When –NH_2 coverage is increased, the charge transfer from LiPSs to the –NH_2 groups approximately doubles compared to that in the 1–NH_2 system. This corresponds to a massive increase in adsorption energy, representing overly strong binding that can trap polysulfides and impede desorption. Interestingly, while the charge transfer to the –NH_2 groups scales with coverage, the charge transfer to the underlying bilayer surface remains relatively stable, highlighting that the functional groups are the primary drivers of this regulation.

2.3 | Electrochemical Performance and Redox Kinetics

The influence of BN incorporation and NH_2 functionalization on sulfur utilization was systematically evaluated to clarify the

balance between polarity and electronic transport. As shown in Figure 4a, introducing BN at a moderate ratio (BN/CNT = 1:4) increases the initial discharge capacity from 864 mAh g^{-1} (CNT) to 963 mAh g^{-1}, indicating improved sulfur utilization associated with the introduction of polar domains. After 200 cycles, the capacities remain at 767 and 831 mAh g^{-1} for the CNT and BN/CNT (1:4), respectively. To assess whether further increasing the BN content enhances the performance, a higher loading (BN/CNT = 1:1) was examined (Figure S12). Despite the increased polarity, the 1:1 electrode delivers an initial capacity of 863 mAh g^{-1} and retains a capacity of 752 mAh g^{-1} after 200 cycles, which is slightly less than that retained by the pristine CNT under identical conditions. These results suggest that excessive BN loading does not further improve sulfur utilization and may instead compromise electrochemical performance because of disrupted electronic pathways.

The polarization behavior provides further insight. CV curves (Figures 4b and S13) were analyzed by separating the upper ($S_8 \rightarrow Li_2S_4$) and lower ($Li_2S_4 \rightarrow Li_2S_2/Li_2S$) plateau reactions [20]. For the BN/CNT (1:1), the peak-to-peak voltage gaps are $\Delta E_{p\,(upper)}$ = 0.43 V and $\Delta E_{p\,(lower)}$ = 0.73 V, both of which are larger than those of the BN/CNT (1:4) (0.35 and 0.64 V) and CNT (0.18 and 0.45 V). The oxidation peak shifts to 2.60 V, indicating aggravated polarization. These observations suggest that excessive BN loading likely disrupts conductive pathways and increases interfacial resistance, despite its polar nature. In contrast, BN–NH_2/CNT delivers a significantly higher initial capacity of 1089 mAh g^{-1} and retains a capacity of 909 mAh g^{-1} after 200 cycles (Figure 4a). To further evaluate its long-term cycling stability, the BN–NH_2/CNT electrode was tested at 0.2C with an E/S ratio of 10.3 µL mg^{-1} (Figure 4c). The electrode maintained 1150 mAh g^{-1} after 500 cycles, corresponding to 87.1% of its initial capacity. The voltage profiles (Figure 4d–f) reveal that the charge–discharge voltage gap (ΔV) decreases to 0.19 V after 150 cycles, compared with the 0.26 V charge–discharge voltage gap for the CNT and the 0.30 V charge–discharge voltage gap for the BN/CNT (1:4). The reduced polarization indicates improved redox reversibility during prolonged cycling. Quantitative analysis of the CV curves further supported this trend. For the BN–NH_2/CNT, the $\Delta E_{p\,(upper)}$ and $\Delta E_{p\,(lower)}$ values decrease to 0.12 and 0.37 V, respectively, both of which are markedly lower than those of the BN/CNT and CNT. Notably, the oxidation peak shifts to a much lower potential (2.37 V), whereas the lower reduction peak shifts positively to 2.00 V. These shifts suggest facilitated kinetics for both Li_2S formation and decomposition. These results are consistent with moderated interfacial interactions that retain soluble polysulfide species near the conductive framework while preserving dynamic adsorption–desorption behavior, thereby avoiding overly strong binding that could impede redox reversibility [21, 22].

The conversion of high-order polysulfides was further examined by analyzing the capacity contribution of the upper discharge plateau ($S_8 \rightarrow Li_2S_4$), corresponding to a theoretical capacity of 419 mAh g^{-1} [23, 24]. As shown in Figure 4g–i, the capacity of the BN–NH_2/CNT reaches 419 mAh g^{-1} in the first cycle, indicating the near-complete utilization of dissolved long-chain polysulfides. Although the BN/CNT substrate (1:4) initially achieves a capacity of 392 mAh g^{-1}, its upper plateau capacity decreases to 289 mAh g^{-1} after 150 cycles, which is comparable to that of the CNT (282 mAh g^{-1}). In contrast, the BN–NH_2/CNT substrate retains 330 mAh g^{-1} after 150 cycles, demonstrating the sustained confinement and conversion efficiency of soluble polysulfide intermediates. These results indicate that sulfur host engineering requires a careful balance between polarity and electronic transport [6]. Excessive BN incorporation introduces kinetic polarization by partially disrupting the conductive CNT framework, whereas an optimized BN architecture combined with NH_2 functionalization establishes moderated electrostatic regulation at the heterointerface. This configuration preserves the conductive network while promoting reversible polysulfide/Li_2S conversion. As a result, sulfur utilization is effectively improved in the BN–NH_2/CNT design, suggesting that the kinetic barriers associated with electrochemical reactions in lithium–sulfur batteries are properly reduced.

Following the analysis of upper-plateau sulfur utilization, the kinetics of the lower-plateau reaction ($Li_2S_4 \rightarrow Li_2S$) were examined using potentiostatic Li_2S precipitation tests (Figure 4j–l) [25, 26]. Under identical electrochemical conditions, distinct nucleation behaviors were observed among the three electrodes. The peak time (T_p), corresponding to the onset of rapid Li_2S nucleation and growth, decreases from 1200 s for the CNT to 488 s for the BN/CNT, suggesting that the introduction of BN facilitates Li_2S nucleation. The BN–NH_2/CNT substrate has a similarly shortened T_p of 575 s, which is slightly longer than that of the BN/CNT, suggesting a moderated nucleation behavior rather than excessively rapid precipitation. More importantly, compared with those of the CNT (419 mAh g^{-1}) and BN/CNT (422 mAh g^{-1}), the integrated Li_2S precipitation capacity increases markedly for BN–NH_2/CNT (548 mAh g^{-1}). While BN incorporation primarily accelerates nucleation, NH_2 functionalization enables more sustained Li_2S growth before impingement, resulting in a higher overall deposition capacity. These results indicate that the BN–NH_2/CNT substrate not only facilitates Li_2S formation but also maintains an effective three-phase boundary for continued conversion, thereby enhancing the reversibility of the lower plateau reaction.

To probe the kinetic implications of the optimized BN framework and NH_2 functionalization, the rate performance was evaluated at increasing current densities (Figure 5a). At 1C, the discharge capacities are 740, 818, and 897 mAh g^{-1} for the CNT, BN/CNT (1:4), and BN–NH_2/CNT, respectively. At 2C, the capacities decrease to 634, 679, and 790 mAh g^{-1}, demonstrating a pronounced high-rate advantage for the BN–NH_2/CNT. The galvanostatic profiles reveal consistently smaller voltage gaps (ΔV) for the BN–NH_2/CNT across different C rates (Figure 5b,c), indicating reduced polarization under kinetically demanding conditions.

To further examine the origin of the improved rate performance, EIS analysis was performed (Figures 5d–i and S14). Before cycling, the charge-transfer resistance (R_{ct}) decreases from 150.2 Ω (CNT) to 88 Ω (BN/CNT) and 60.3 Ω (BN–NH_2/CNT). After 50 cycles, the BN–NH_2/CNT substrate maintains the lowest R_{ct} (4.8 Ω), compared with the R_{ct} of 15.2 Ω for BN/CNT and that of 9.7 Ω for the CNT. The interfacial resistance component (R_{int}) remains substantially greater for the CNT (~105 Ω) than for the BN-containing electrodes (~14–15 Ω) after 50 cycles, suggesting more

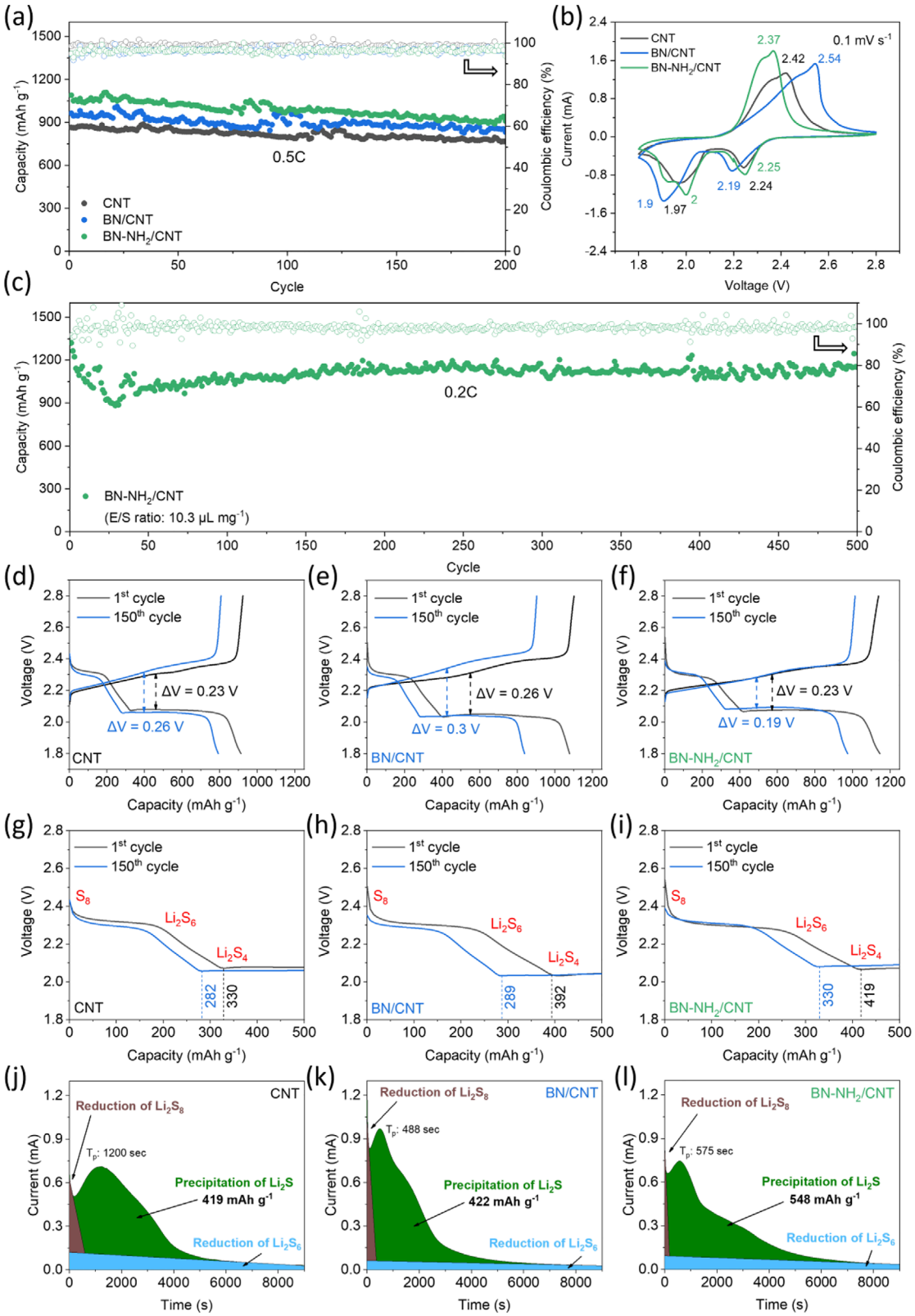


FIGURE 4 | (a) Cycling performance of Li–S cells at 0.5C with the CNT, BN/CNT (1:4), and BN–NH_2/CNT cathode substrates with an electrolyte/sulfur (E/S) ratio of 31 μL mg^{-1}. (b) CV curves at 0.1 mV s^{-1} for the CNT, BN/CNT (1:4), and BN–NH_2/CNT cathode substrates. (c) Long-term cycling performance of the Li–S cell at 0.2C with the BN–NH_2/CNT cathode substrate over 500 cycles with an E/S ratio of 10.3 μL mg^{-1}. (d–f) Galvanostatic charge–discharge profiles at the first and 150th cycles, with corresponding voltage gap (ΔV) values. Capacity contribution of the upper discharge plateau ($S_8 \rightarrow Li_2S_4$) at the first and 150th cycles for the (g) CNT, (h) BN/CNT (1:4), and (i) BN–NH_2/CNT cathode substrates. The theoretical capacity for this reaction step is 419 mAh g^{-1}. Potentiostatic Li_2S precipitation tests for the (j) CNT, (k) BN/CNT, and (l) BN–NH_2/CNT cathode substrates under identical electrochemical conditions. The peak time (T_p) corresponds to the maximum Li_2S precipitation rate.

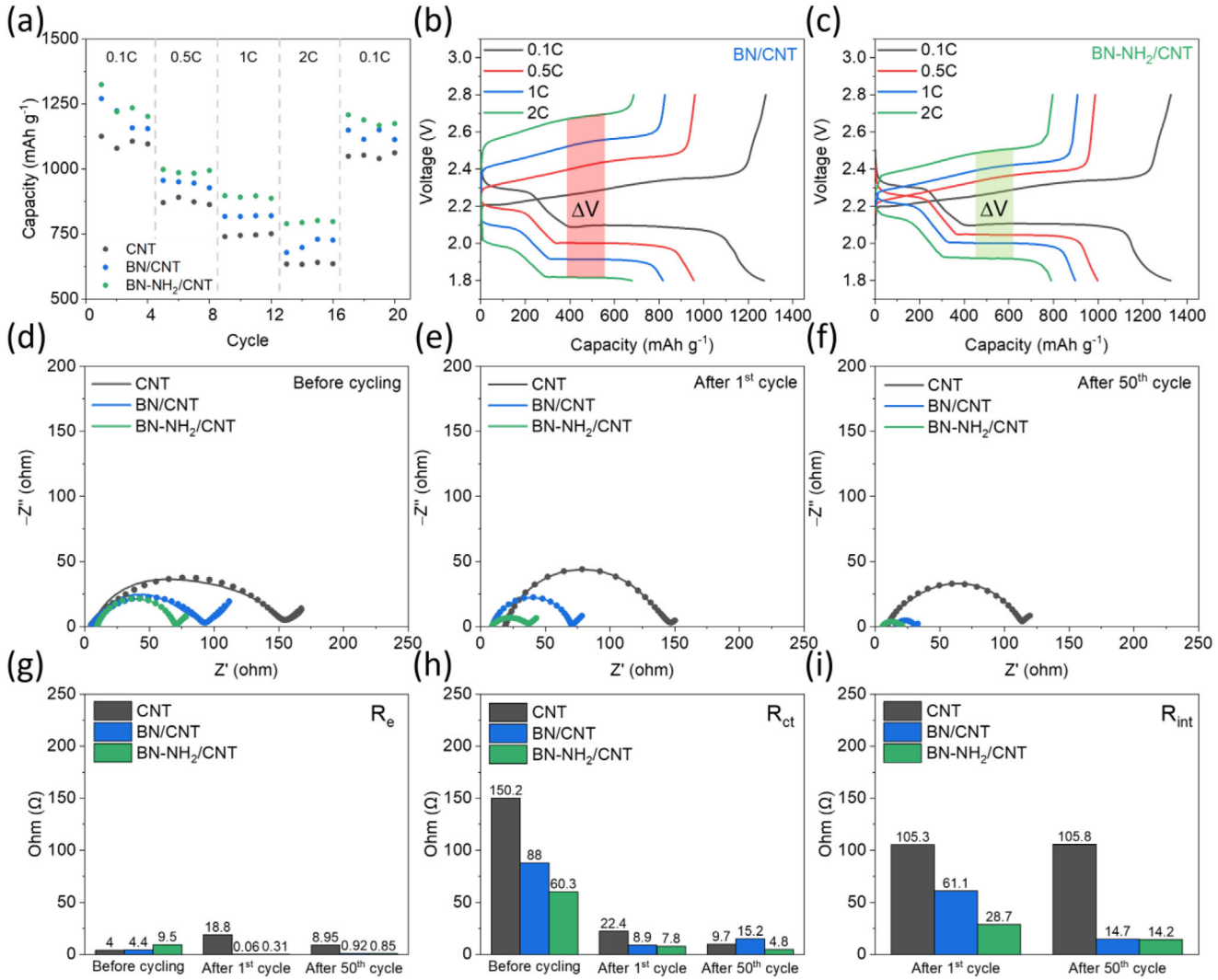


FIGURE 5 | (a) Rate capability of the CNT, BN/CNT (1:4), and BN–NH_2/CNT cathode substrates at different current densities. (b–c) Representative charge–discharge profiles at various C rates, highlighting the voltage gap (ΔV). Nyquist plots (d) before cycling, (e) after the first cycle, and (f) after the 50^{th} cycle for the CNT, BN/CNT (1:4), and BN–NH_2/CNT cathode substrates. (g–i) Corresponding resistance values (R_e, R_{ct}, and R_{int}) are summarized in the bar charts.

pronounced impedance accumulation in the absence of BN-based interfacial modification. The consistently lower R_{ct} and reduced polarization for BN–NH_2/CNT indicate that the engineered heterointerface facilitates charge transfer processes, which is consistent with the proposed interfacial electronic modulation and improved charge transfer processes.

2.4 | Postcycling Structural Evolution and Electronic Regulation of Sulfur Deposition

To elucidate the structural consequences of interfacial regulation after cycling, cross-sectional and surface SEM analyses were conducted. Representative cross-sectional SEM images are presented in Figure 6a–d, while additional images obtained at different positions and the corresponding thickness statistics are provided in Figure S15. Based on measurements at multiple positions, the mean thickness of the CNT electrode increased substantially from 38.1 to 56.2 μm after cycling, corresponding to an increase of approximately 48%. In contrast, the mean thicknesses of the BN/CNT and BN–NH_2/CNT electrodes remained nearly unchanged. These results demonstrate that both BN-based interlayers effectively suppressed the pronounced postcycling electrode thickening observed for the CNT electrode. EDS mapping clarified the compositional distribution across the electrode cross-sections. In Figure 6c,d, the upper region of the BN/CNT electrode clearly shows B and N signals, corresponding to the BN layer, whereas the underlying region is dominated by C signals from the CNT framework, confirming the preserved bilayer architecture after cycling. In both the CNT and BN/CNT electrodes after cycling, distinct S signals are detected within the electrode structure (Figure 6b,d), confirming the presence of sulfur species retained within the electrode structure after cycling. Surface SEM images provide additional insight into the deposition morphology. After cycling, the CNT electrode becomes covered by a continuous and relatively thick surface layer, as evidenced by the strong S signal distributed across the surface and the markedly weakened C signal (Figure 6e), indicating that

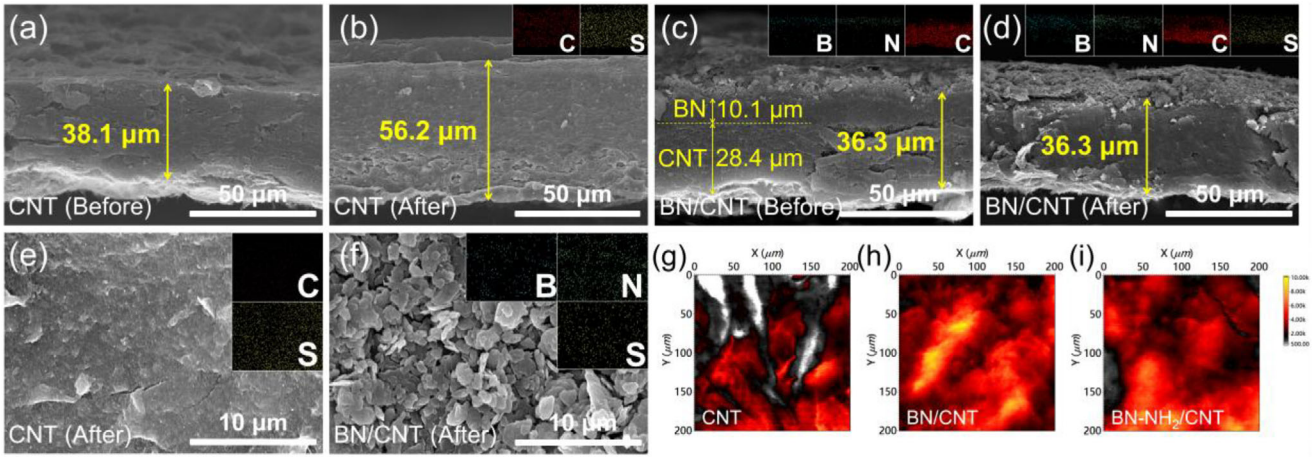


FIGURE 6 | Analysis of the structure and composition of the Li–S electrodes after cycling. Cross-sectional SEM images of the CNT (a) before and (b) after cycling, showing a pronounced increase in thickness after cycling. Cross-sectional SEM images of the BN/CNT (c) before and (d) after cycling, revealing that the thickness and bilayer architecture are essentially maintained. The corresponding EDS elemental mapping confirms that the upper region of the BN/CNT is enriched in B and N (BN layer), whereas the underlying region is dominated by C from the CNT framework. In the cycled electrodes, distinct S signals are detected across the cross-sections, confirming sulfur retention within the electrode structures. (e) Surface SEM image and corresponding EDS mapping of the cycled CNT, showing a thick sulfur layer across the surface and the appearance of weakened C signals. (f) Surface SEM image and EDS mapping of the cycled BN/CNT, where sulfur is distributed across the surface while the B and N signals remain detectable, indicating that BN is preserved at the interface after cycling. Nano-XRF sulfur mapping of the cycled (g) CNT, (h) BN/CNT, and (i) BN–NH_2/CNT electrodes, demonstrating a spatially heterogeneous sulfur distribution on the CNT and a comparatively uniform sulfur distribution on the BN/CNT and BN–NH_2/CNT.

the deposited sulfur species substantially cover the underlying carbon framework. Such extensive surface coverage is consistent with the extremely high interfacial resistance observed in the EIS analysis of the CNT electrode (Figure 5i), suggesting that the thick sulfur layer may impede efficient charge transfer across the electrode–electrolyte interface. In comparison, the surface of the BN/CNT electrode is covered with sulfur; however, the original B and N signals remain clearly detectable, and the surface morphology remains unchanged (Figure 6f), suggesting that sulfur deposition does not completely obscure the BN layer and that excessive surface film formation is inhibited.

To further evaluate the spatial distribution of sulfur species, nano-XRF mapping was performed (Figure 6g–i). The CNT electrode has a heterogeneous sulfur distribution across its surface, with noticeable spatial variation in signal intensity, indicating uneven deposition after cycling. In contrast, the mapping results of the BN/CNT and BN–NH_2/CNT substrates exhibit a clearer and more uniform and continuous sulfur signal distributed across the scanned region, suggesting more homogeneous sulfur adsorption behavior. Intensity distributions derived from all 40000 data points within each 200 × 200 μm^2 mapping area further confirm the greater prevalence of low-intensity regions in the CNT electrode (Figure S16). These combined structural and compositional observations suggest that BN incorporation promotes more spatially regulated sulfur distribution, thereby mitigating localized accumulation and contributing to the minimal macroscopic thickness change observed during cycling.

Additionally, XAS was performed to investigate the electronic environment of sulfur species after cycling (Figure 7a). Both the BN/CNT and BN–NH_2/CNT substrates exhibit similar spectral profiles, with low-energy sulfur features at ~2472.2–2472.8 eV and a strong white-line region near ~2480 eV that is associated with electrolyte-derived sulfur environments such as LiTFSI [27]. Despite the comparable line shapes, compared with the BN/CNT profile, the BN–NH_2/CNT profile displays a feature at ~2472 eV with a higher relative intensity, which is reflected by the larger ratio between the intensities of the active sulfur peak and the $TFSI^-$ region ($R = I_{S_x^{2-}}/I_{TFSI^-}$, 0.435 vs. 0.174). This increase suggests a greater relative contribution of electrochemically active sulfur species at the BN–NH_2/CNT interface. Although both samples were measured under the same electrochemical conditions, their divergent sulfur-conversion behavior may result in different relative populations of Li_2S and residual LiPS species. Therefore, the intensity difference may reflect differences in sulfur speciation as well as interfacial electronic interactions. A magnified view of the low-energy region (Figure 7b) further reveals that the ~2472 eV feature of the BN–NH_2/CNT shifts by ~0.54 eV toward lower photon energy relative to that of the BN/CNT. This subtle energy shift may reflect differences in sulfur speciation and changes in the local electronic environment. Electronic screening arising from interactions between sulfur species and the NH_2-functionalized interface may contribute to the shift; however, the respective contributions cannot be quantitatively distinguished without appropriate sulfur reference spectra and linear-combination analysis. Accordingly, the XAS results indicate altered sulfur speciation and local electronic environments at the BN–NH_2/CNT interface rather than exclusively increased local electron density.

Furthermore, to examine the interfacial chemical evolution after cycling, XPS N 1s spectra were compared for the BN/CNT and BN–NH_2/CNT electrodes (Figures 7c,d and S17). Both electrodes exhibit the characteristic N–B component associated with the BN framework. Notably, only the BN–NH_2/CNT electrode

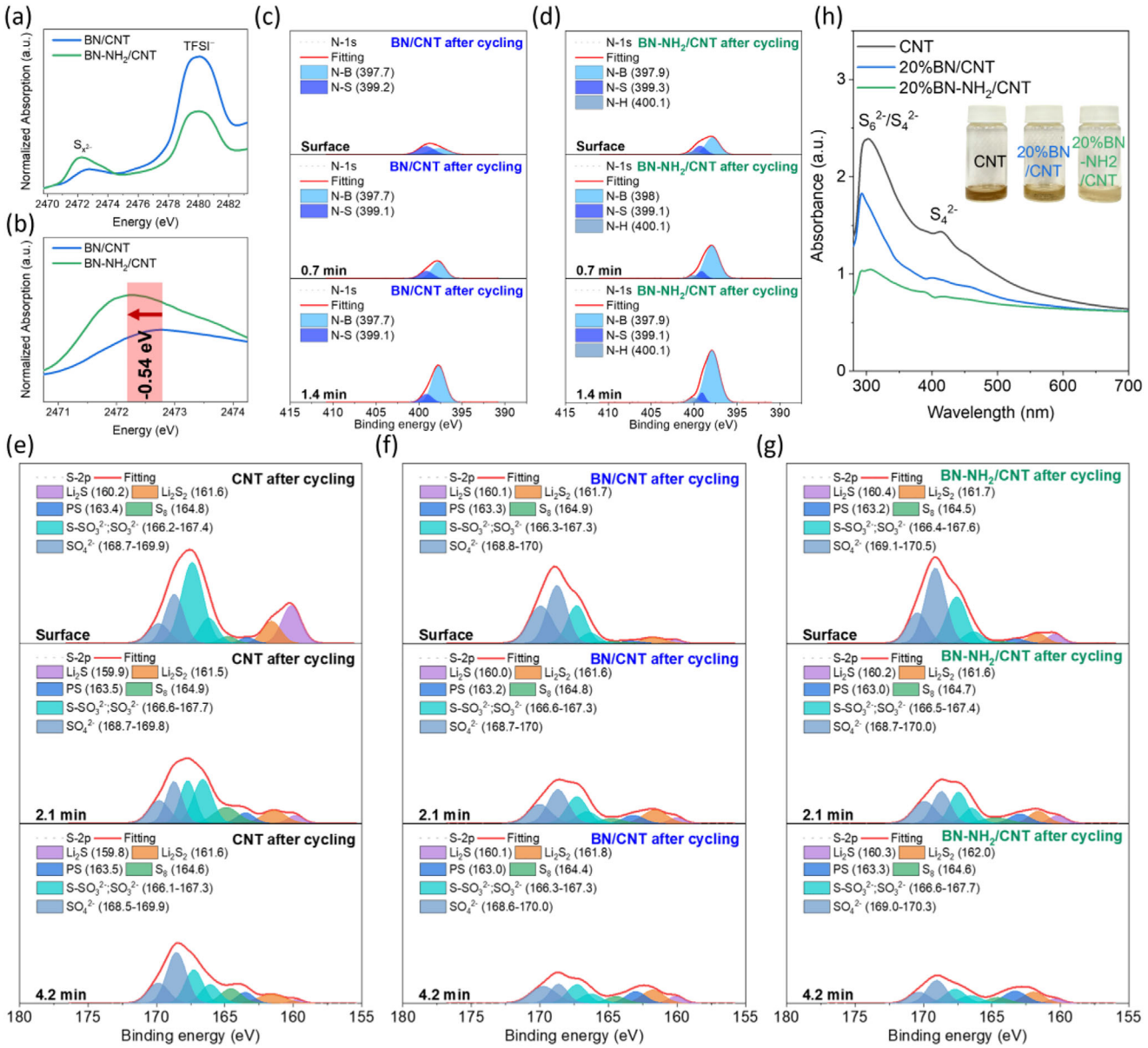
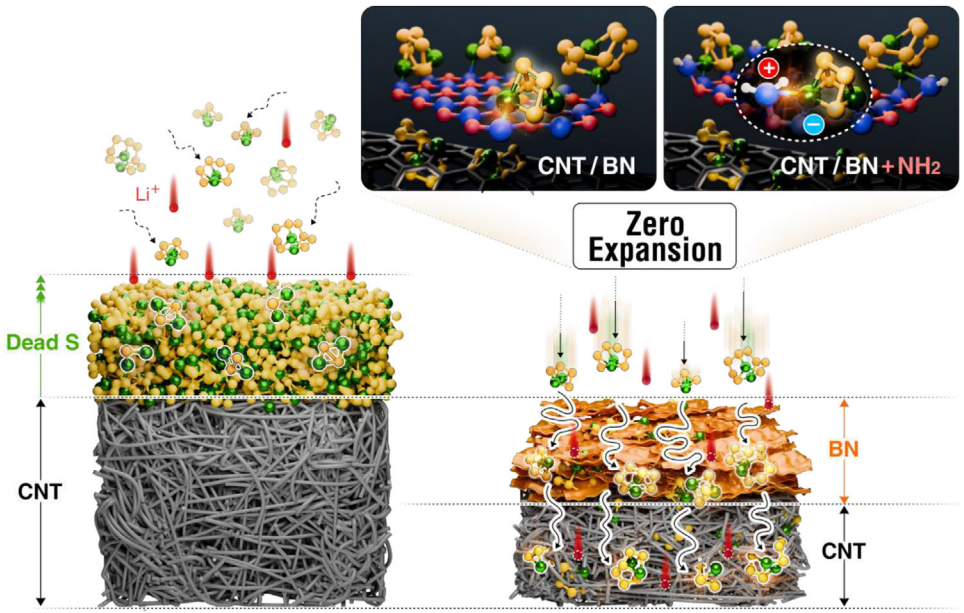


FIGURE 7 | Electronic structure and interfacial chemical evolution of sulfur species after cycling. (a) Normalized S K-edge XAS spectra of the BN/CNT and BN–NH_2/CNT electrodes collected in the discharged state. Both electrodes exhibit similar spectral profiles, with a low-energy sulfur feature near ~2472 eV and a strong white-line feature at ~2480 eV that is associated with electrolyte-related sulfur species. (b) Enlarged view of the low-energy sulfur region, highlighting the ~0.54 eV energy downshift and enhanced relative intensity observed for the BN–NH_2/CNT. N 1s XPS spectra of the (c) BN/CNT and (d) BN–NH_2/CNT electrodes after cycling, showing the preserved BN framework signals and enhanced N–S-related interactions in the BN–NH_2/CNT. (e–g) Depth-profiled S 2p XPS spectra revealing the distribution of Li_2S, Li_2S_2, polysulfides, and oxidized sulfur species across the surface and subsurface regions. (h) UV–Vis spectra of the electrolytes extracted from the cycled Li–S cells with the CNT, BN/CNT, and BN–NH_2/CNT cathodes. Compared with those of the CNT, the intensities of the characteristic polysulfide absorption peaks of the BN/CNT and BN–NH_2/CNT substrates at ~300 and ~410 nm decrease, indicating a reduced dissolved polysulfide concentration.

displays a distinct N–H-related signal, confirming the presence of amine-related functionality after cycling. In addition, an N–S-related component (~399.1 eV) is observed for both the BN/CNT and BN–NH_2/CNT electrodes [28]. The N–S signature suggests that the top BN layer and the introduced amine groups promote increased interfacial interactions with sulfur species during cycling. Rather than indicating irreversible chemical bonding, this feature is consistent with increased interfacial coupling between nitrogen-containing sites and polysulfide species. Notably, the intensity of the surface signal prior to sputtering is partially attenuated, likely because of coverage by electrolyte-derived oxidized species formed during cycling. The coexistence of persistent N–H functionality and enhanced N–S interactions implies that NH_2 functionalization provides accessible polar sites that promote moderated electrostatic regulation of sulfur species.

The chemical states of sulfur species after cycling were further analyzed by XPS S 2p spectra with depth profiling (Figures 7e–g and S18). The fitted spectra exhibit characteristic



SCHEME 1 | Schematic illustration of interfacial electrostatic regulation in BN-based heterostructures for lithium–sulfur batteries. The BN framework promotes spatially stabilized sulfur redox chemistry by suppressing localized surface accumulation and maintaining a dimensionally stable cathode architecture. Subsequent NH_2 functionalization introduces moderated electrostatic regulation at the heterointerface, enabling balanced polysulfide interactions, enhanced active sulfur utilization, and controlled Li_2S nucleation and growth.

peaks at ~160.1 eV for Li_2S, ~161.8 eV for Li_2S_2, ~163 eV for polysulfides (PS), and ~164.4 eV for S_8 [23]. The peaks at ~166.1–167.7 eV correspond to the oxidized sulfur species, including sulfite ($[SO_3]^{2-}$) and lithium thiosulfate ($[S–SO_3]^{2-}$); these peaks likely originate from the reduction products of LiTFSI and $LiNO_3$ [23]. The broad feature at ~168.5–170.5 eV corresponds to sulfate ($[SO_4]^{2-}$) species formed via side reactions during cycling [23]. Depth-dependent analysis revealed distinct distribution patterns among the electrodes. With respect to the CNT, the outer surface region contains significantly greater proportions of Li_2S and Li_2S_2, indicating substantial accumulation of reduced active sulfur species near the electrode surface. This observation is consistent with the insulating and thick sulfur layer observed in postcycling EIS and SEM analyses (Figures 5i and 6e), suggesting that surface-dominated deposition may hinder subsequent ion and electron transport pathways. In contrast, both the BN/CNT and BN–NH_2/CNT electrodes exhibit a more balanced distribution of active sulfur species across the surface and subsurface regions. The relative proportions of Li_2S, Li_2S_2, and polysulfides remain more evenly distributed throughout the depth profile, indicating the mitigation of surface overaccumulation and a more balanced distribution of active sulfur species within the electrode architecture. Notably, compared with the BN/CNT electrode, the BN–NH_2/CNT electrode has a slightly more uniform compositional distribution, suggesting that NH_2 functionalization further contributes to the interfacial regulation of sulfur conversion. To further evaluate sulfur retention after prolonged cycling, the electrolyte extracted from the cycled cells was analyzed by UV–Vis spectroscopy (Figure 7h). The absorbance intensity of the CNT electrode is the highest in the characteristic polysulfide regions (~300 and ~410 nm) [3], indicating substantial dissolution of active sulfur species during cycling. In contrast, the absorbance of the BN/CNT is reduced, whereas that of the BN–NH_2/CNT is the lowest across the entire wavelength range. The suppressed signal suggests that NH_2 functionalization more effectively limits polysulfide migration and mitigates active sulfur loss.

On the basis of the combined structural, electrochemical, and spectroscopic analyses, a mechanistic illustration is proposed to summarize the interfacial regulation behavior of the BN-based heterostructures (Scheme 1). For the BN/CNT configuration, the introduction of a polar BN framework promotes spatially stabilized sulfur redox chemistry. The preserved bilayer architecture and balanced sulfur distribution observed by SEM, nano-XRF, and depth-profiled XPS indicate that BN incorporation mitigates the localized surface overaccumulation of reduced sulfur species. This regulation enables more homogeneous active sulfur redistribution throughout cycling, thereby maintaining a dimensionally stable cathode structure with negligible macroscopic swelling. Upon further amine functionalization, the BN–NH_2/CNT heterostructure introduces moderated electrostatic regulation at the interface. Electronic structure analysis (XAS and XPS) suggested changes in sulfur speciation and the local electronic environment arising from interfacial interactions. This moderated interaction results in the retention of soluble polysulfide intermediates near the conductive framework while preserving the dynamic adsorption–desorption behavior. As a result, active sulfur utilization is significantly improved, which is accompanied by facilitated Li_2S nucleation and sustained growth under controlled spatial confinement. Representative BN-based sulfur hosts are compared in Table S1. Previous designs regulate sulfur chemistry primarily through vacancy engineering, conductive hybridization, physical confinement, or catalytic components. In contrast, the BN–NH_2/CNT substrate employs a spatially separated bilayer architecture with distinct functional roles: the NH_2-functionalized BN upper layer regulates LiPS retention and sulfur deposition, whereas the

underlying CNT network provides continuous electron transport. This functional separation distinguishes the present sulfur spatial regulation strategy from conventional BN-based composite hosts.

3 | Conclusions

In summary, we demonstrate that the coordinated interfacial engineering of BN-based heterostructures enables the simultaneous regulation of sulfur spatial distribution and redox kinetics in lithium–sulfur batteries. The BN framework establishes spatially stabilized sulfur redox chemistry by mitigating surface-dominated accumulation and maintaining a dimensionally stable cathode architecture with negligible macroscopic swelling. Building upon this structural stabilization, amine functionalization introduces moderated electrostatic regulation at the heterointerface. Density functional theory calculations reveal localized electronic polarization and tuned interfacial interaction strength, whereas spectroscopic analyses indicate changes in sulfur speciation and local electronic environments associated with the engineered interface. This balanced interaction retains soluble polysulfide species near the conductive network while preserving dynamic adsorption–desorption behavior, thereby enhancing active sulfur utilization and supporting regulated Li_2S nucleation and conversion behavior. Rather than relying on the strong chemical trapping of polysulfides, this work highlights the importance of controlled electrostatic modulation to balance interfacial interactions and charge transport. The synergistic integration of spatial regulation and electronic tuning establishes a kinetically favorable and dimensionally stable Li–S cathode architecture. More broadly, this study provides a general interfacial design principle for conversion-type energy storage systems where moderated interactions facilitate reversible redox chemistry.

Acknowledgements

This research was supported by the National Science and Technology Council (NSTC), Taiwan (114-2628-E-A49-013-MY4 and 113-2113-M-003-008), and by the Ministry of Education (MOE), Taiwan, under the Yushan Young Fellow Program (MOE-114-YSFEE-0010-005-P2) and the Higher Education SPROUT Project at National Yang Ming Chiao Tung University. We thank Ms. Swee-Lan Cheah (Instrumentation Center, National Tsing Hua University) for assistance with HRXPS analysis, Prof. Niall Tumilty for support with UV–Vis measurements, and Dr. Ying-Rui Lu for processing the XAS data. We also acknowledge the National Synchrotron Radiation Research Center (NSRRC), Taiwan, for providing the synchrotron radiation facilities (TPS 21A/32A) and technical support, and the National Center for High-Performance Computing (NCHC) in Taiwan for computational resources.

Conflicts of Interest

The authors declare no conflicts of interest.

Data Availability Statement

The data that support the findings of this study are available from the corresponding author upon reasonable request.

References

1. A. Manthiram, Y. Fu, and Y.-S. Su, "Challenges and Prospects of Lithium–Sulfur Batteries," *Accounts of Chemical Research* 46 (2013): 1125–1134, https://doi.org/10.1021/ar300179v.

2. L. Zhou, D. L. Danilov, R. Eichel, and P. H. L. Notten, "Host Materials Anchoring Polysulfides in Li–S Batteries Reviewed," *Advanced Energy Materials* 11 (2021): 2001304, https://doi.org/10.1002/aenm.202001304.

3. K. Chiu, A. L. Bhat, C. Yang, S. Chung, N. Tumilty, and Y. Su, "Advanced Li–S Battery Configuration Featuring Sulfur-Coated Separator and Interwoven rGO/CNT Fabric Current Collector," *Small* 21 (2024): 2405365, https://doi.org/10.1002/smll.202405365.

4. S. Waluś, G. Offer, I. Hunt, et al., "Volumetric Expansion of Lithium-Sulfur Cell during Operation – Fundamental Insight into Applicable Characteristics," *Energy Storage Materials* 10 (2018): 233–245, https://doi.org/10.1016/j.ensm.2017.05.017.

5. C. Li, X. Liu, L. Zhu, et al., "Conductive and Polar Titanium Boride as a Sulfur Host for Advanced Lithium–Sulfur Batteries," *Chemistry of Materials* 30 (2018): 6969–6977, https://doi.org/10.1021/acs.chemmater.8b01352.

6. B. Lee, T. Kang, H. Lee, et al., "Revisiting the Role of Conductivity and Polarity of Host Materials for Long-Life Lithium–Sulfur Battery," *Advanced Energy Materials* 10 (2020): 1903934, https://doi.org/10.1002/aenm.201903934.

7. Q. Liang, S. Wang, Y. Yao, P. Dong, and H. Song, "Transition Metal Compounds Family for Li–S Batteries: The DFT-Guide for Suppressing Polysulfides Shuttle," *Advanced Functional Materials* 33 (2023): 2300825, https://doi.org/10.1002/adfm.202300825.

8. W. Zhang, H. Pan, N. Han, et al., "Balancing Adsorption, Catalysis, and Desorption in Cathode Catalyst for Li–S Batteries," *Advanced Energy Materials* 13 (2023): 2301551, https://doi.org/10.1002/aenm.202301551.

9. S. Deng, T. Guo, and J. Heier, "Unraveling Polysulfide's Adsorption and Electrocatalytic Conversion on Metal Oxides for Li-S Batteries," *Advanced Science* 10 (2023): 2204930, https://doi.org/10.1002/advs.202204930.

10. T. Nguyen and Y.-S. Su, "A Self-Assembled Carbon Nanotube/Silicon Composite Battery Anode Stabilized with Chemically Reduced Graphene Oxide Sheets," *Materials & Design* 240 (2024): 112861, https://doi.org/10.1016/j.matdes.2024.112861.

11. Y.-S. Su, Y. Fu, and A. Manthiram, "Self-Weaving Sulfur–carbon Composite Cathodes for High Rate Lithium–sulfur Batteries," *Physical Chemistry Chemical Physics* 14 (2012): 14495, https://doi.org/10.1039/c2cp42796f.

12. X. Ma, N.-H. Lee, H.-J. Oh, S.-C. Jung, W.-J. Lee, and S.-J. Kim, "Morphology Control of Hexagonal Boron Nitride by a Silane Coupling Agent," *Journal of Crystal Growth* 316 (2011): 185–190, https://doi.org/10.1016/j.jcrysgro.2010.12.066.

13. L. Hua Li, Y. Chen, B.-M. Cheng, M.-Y. Lin, S.-L. Chou, and Y.-C. Peng, "Photoluminescence of Boron Nitride Nanosheets Exfoliated by Ball Milling," *Applied Physics Letters* 100 (2012): 261108, https://doi.org/10.1063/1.4731203.

14. R. Rizvi, E. P. Nguyen, M. D. Kowal, et al., "High-Throughput Continuous Production of Shear-Exfoliated 2D Layered Materials Using Compressible Flows," *Advanced Materials* 30 (2018): 1800200, https://doi.org/10.1002/adma.201800200.

15. L. An, Y. Yu, C. Bai, et al., "Simultaneous Production and Functionalization of Hexagonal Boron Nitride Nanosheets by Solvent-Free Mechanical Exfoliation for Superlubricant Water-Based Lubricant Additives," *npj 2D Materials and Applications* 3 (2019): 28, https://doi.org/10.1038/s41699-019-0111-9.

16. W. Lei, V. N. Mochalin, D. Liu, S. Qin, Y. Gogotsi, and Y. Chen, "Boron Nitride Colloidal Solutions, Ultralight Aerogels and Freestanding Membranes through One-Step Exfoliation and Functionalization," *Nature Communications* 6 (2015): 8849, https://doi.org/10.1038/ncomms9849.

17. K. S. Kim, C. T. Kingston, A. Hrdina, et al., "Hydrogen-Catalyzed, Pilot-Scale Production of Small-Diameter Boron Nitride Nanotubes and Their Macroscopic Assemblies," *ACS Nano* 8 (2014): 6211–6220, https://doi.org/10.1021/nn501661p.

18. N. Chalmpes, A. B. Bourlinos, A. W. Alsmaeil, et al., "First Synthesis of 2D Materials by Hypergolic Reactions and Evaluation of Their Dispersions for Ink Formulation: Hexagonal Boron Nitride and Fluorinated Carbon Nanosheets," *Materials Research Express* 11 (2024): 035002, https://doi.org/10.1088/2053-1591/ad2d42.

19. Y. Yi, H. Li, H. Chang, et al., "Few-Layer Boron Nitride with Engineered Nitrogen Vacancies for Promoting Conversion of Polysulfide as a Cathode Matrix for Lithium–Sulfur Batteries," *Chemistry—A European Journal* 25 (2019): 8112–8117, https://doi.org/10.1002/chem.201900884.

20. Y.-S. Su and A. Manthiram, "Lithium–sulphur Batteries with a Microporous Carbon Paper as a Bifunctional Interlayer," *Nature Communications* 3 (2012): 1166, https://doi.org/10.1038/ncomms2163.

21. Z. Shen, X. Jin, J. Tian, et al., "Cation-Doped ZnS Catalysts for Polysulfide Conversion in Lithium–sulfur Batteries," *Nature Catalysis* 5 (2022): 555–563, https://doi.org/10.1038/s41929-022-00804-4.

22. W.-G. Lim, S. Kim, M. Kim, et al., "Understanding the Electrocatalytic Trend of Sulfur Reduction Reaction and Design Rules of Advanced Electrocatalysts for Li–S Batteries," *ACS Nano* 19 (2025): 27318–27331, https://doi.org/10.1021/acsnano.5c05200.

23. N. L. Le, S.-L. Hsu, T. H. Vu, et al., "Transformation of Polysulfide Catholyte Chemistry through Lithium-Arene Complexes for Superior Solubility and Cyclability in Li–S Batteries," *JACS Au* 5 (2025): 3866–3878, https://doi.org/10.1021/jacsau.5c00537.

24. Y. Su, Y. Fu, B. Guo, S. Dai, and A. Manthiram, "Fast, Reversible Lithium Storage with a Sulfur/Long-Chain-Polysulfide Redox Couple," *Chemistry—A European Journal* 19 (2013): 8621–8626, https://doi.org/10.1002/chem.201300886.

25. F. Y. Fan, W. C. Carter, and Y. Chiang, "Mechanism and Kinetics of Li_2S Precipitation in Lithium–Sulfur Batteries," *Advanced Materials* 27 (2015): 5203–5209, https://doi.org/10.1002/adma.201501559.

26. J. Sun, Y. Liu, L. Liu, et al., "Interface Engineering toward Expedited Li_2S Deposition in Lithium–Sulfur Batteries: A Critical Review," *Advanced Materials* 35 (2023): 2211168, https://doi.org/10.1002/adma.202211168.

27. L. Jia, J. Wang, S. Ren, et al., "Unraveling Shuttle Effect and Suppression Strategy in Lithium/Sulfur Cells by in Situ/Operando X-ray Absorption Spectroscopic Characterization," *Energy & Environmental Materials* 4 (2021): 222–228, https://doi.org/10.1002/eem2.12152.

28. K. Sun, P. Guo, X. Shang, et al., "Mesoporous Boron Carbon Nitride/Graphene Modified Separators as Efficient Polysulfides Barrier for Highly Stable Lithium-Sulfur Batteries," *Journal of Electroanalytical Chemistry* 842 (2019): 34–40, https://doi.org/10.1016/j.jelechem.2019.04.047.

Supporting Information

Additional supporting information can be found online in the Supporting Information section.

Supporting File: smll75698-sup-0001-SuppMat.docx.